Journal of Electronic Materials (2024) 53:6482–6497
https://doi.org/10.1007/s11664-024-11322-3

ORIGINAL RESEARCH ARTICLE

Polycrystalline T- and H-Nb_2O_5 Thin Films Prepared by Pulsed Laser Deposition: Impact of Laser Fluence

Evan T. Salim[1] · Suhair R. Shafeeq[2] · Mohammed Jalal AbdulRazzaq[3] · Makram A. Fakhri[3] · Ahmad S. Azzahrani[4] · Ali Basem[5] · Forat H. Alsultany[6] · Subash C. B. Gopinath[7,8,9]

Received: 30 April 2024 / Accepted: 9 July 2024 / Published online: 31 July 2024

Abstract

Polycrystalline structures of T-Nb_2O_5 and a remarkable H-Nb_2O_5 structure were successfully obtained in this work. This was achieved using a Nd:YAG laser in a pulsed laser deposition system at laser fluence values of 9.3, 13.4, 16.2, 21, and 25.2 J cm^{-2}. Raman bands of the prepared films are shown and discussed. The optical bandgaps were estimated at 4.81 eV, 4.73 eV, 3.41 eV, 3.29 eV, and 3.21 eV. Photoluminescence (PL) analyses showed agreement with the estimated indirect bandgaps calculated from Tauc's plot for each prepared film. The surface average roughness and root-mean-square (RMS) roughness were also determined and are discussed. The surface morphology as illustrated by field-emission scanning electron microscopy (FE-SEM) reveals the obvious impact of laser energy density on the prepared films. Energy-dispersive x-ray (EDX) analyses revealed the highest stoichiometry attributed to a laser fluence of 21 J cm^{-2}.

Keywords PLD · nanostructures · fine structure · optimum fluence

Introduction

Niobium pentoxide (Nb_2O_5) is an important *n*-type semiconductor, with reported optical bandgap energy of 3.1–5.3 eV.[1–3] It exists primarily in Brazil, Canada, and Nigeria.[4,5] The physicochemical properties of Nb_2O_5 show that it is a highly corrosion-resistant material and possesses the highest thermodynamic stability among Nb oxides.[6–8] Early applications that incorporated Nb_2O_5included catalysts, sensors, and electrochromic materials.[9,10] Nb_2O_5 in the form of thin films and nanostructures is popular in solar cells, batteries, memristors, and other electronics.[11–13] In terms of solid-state capacitors, Nb_2O_5 is the best alternative for tantalum pentoxide ($\varepsilon' = 27$).[14,15] In the field of sensors, it was reported by Hota et al.[16] and Mohammed et al.[17] that Au@Nb_2O_5 can provide good-quality electrodes for both DNA and protein sensors. Nb_2O_5 can also serve as an alternative for biomaterials based on polymers. In the field of dentistry, niobium pentoxide facilitates enhanced adhesive resins.[18–20] Pulsed laser deposition (PLD), first conducted in

✉ Evan T. Salim
evan_tarq@yahoo.com; evan.t.salim@uotechnology.edu.iq

✉ Makram A. Fakhri
mokaram_76@yahoo.com;
makram.a.fakhri@uotechnology.edu.iq

✉ Ahmad S. Azzahrani
ahmad.azzahrani@nbu.edu.sa

[1] Applied Science Department, University of Technology-Iraq, Baghdad 10066, Iraq

[2] Al-Turath University College, Baghdad, Iraq

[3] Laser and Optoelectronic Engineering, University of Technology-Iraq, Baghdad 10066, Iraq

[4] Electrical Engineering Department, Northern Border University, Arar, Saudi Arabia

[5] Air Conditioning Engineering Department, Faculty of Engineering, Warith Al-Anbiyaa University, Karbala 56001, Iraq

[6] Department of Medical Physics, Al-Mustaqbal University College, Babylon, Iraq

[7] Center for Global Health Research, Saveetha Medical College & Hospital, Saveetha Institute of Medical and Technical Sciences (SIMATS), Thandalam, Chennai, Tamil Nadu 602 105, India

[8] Faculty of Chemical Engineering & Technology and Institute of Nano Electronic Engineering, Universiti Malaysia Perlis (UniMAP), 02600 Arau, Perlis, Malaysia

[9] Department of Technical Sciences, Western Caspian University, Baku AZ 1075, Azerbaijan

1965, is a simple method with several advantages as compared with other deposition routes.[21,22] These advantages include the possibility for controlling the growth rate, maintaining the stoichiometric transfer, and selecting the required ablation geometry.[23,24] A schematic of the PLD system is shown in Fig. 1.

For Nb_2O_5 thin films, in 1999, Fu et al.[25] first investigated the electrochemical and electrochromic properties of Nb oxide thin films by PLD utilizing the third-harmonic Nd:YAG laser. In 2011, Ghosh et al. successfully prepared Nb_2O_5 nanoforest films as solar cell photoanodes by PLD using a KrF laser at various background gas pressures.[26] Recently, Fakhri et al.[27] investigated the impact of annealing temperature on the physical properties of Nb_2O_5 films synthesized by a Q-switched Nd:YAG laser in 0 bar vacuum pressure by changing the substrate temperature in each deposition run. In this paper, we investigate the impact of Nd:YAG laser energy density at the fundamental 1064 nm wavelength. The structural, optical, topographical, and morphological properties of the deposited Nb_2O_5 films are investigated. Based on the results, the optimal fluence is determined, which to the best of our knowledge is reported herein for the first time.

Experimental Setup

Quartz and Si wafer (*p*-type 111) substrates were thoroughly cleaned to remove any existing impurities, fingerprints, dust particles, or any other contamination. This process was performed for about 15 min using an ultrasonic device with a mixture of deionized water and ethanol. Ultrapure (99.99%) Nb_2O_5 powder from Merck (Kenilworth, NJ, USA) was pressed under 15 tons, producing a disk-like shape with a diameter of 2.5 cm and height of 0.5 cm. Thin films were obtained by PLD under specific conditions. For this purpose, the fundamental Nd:YAG laser wavelength with 12 cm focal length was chosen. In order to investigate the laser energy density impact, the substrate temperature and the number of pulses were both fixed. The substrate temperature was kept at 350°C and the number of laser pulses was fixed at only 200 pulses per deposition run, which was chosen on the basis of our previously obtained results described in detail elsewhere.[28–30] A fixed frequency of 3 Hz was used for each deposition. A halogen heater was utilized for heating the substrate. The distance between the laser and the deposition chamber was kept at 10 cm. The target–substrate distance was also fixed at 3 cm. The deposition process was performed in a vacuum chamber under pressure of about 10^{-3} mbar. A range of five fluence values was selected, at 9.36 J cm^{-2}, 13.4 J cm^{-2}, 16.27 J cm^{-2}, 21 J cm^{-2}, and 25.2 J cm^{-2}. The PLD system is equipped with a target rotator that is important for the layer-by-layer deposition. Keeping the target at a regular rotation contributes to the even distribution of plume on the substrate, resulting in better thin film growth. The results were obtained utilizing various analytical techniques including x-ray diffraction (XRD), Raman spectroscopy, UV–visible (UV–Vis) and photoluminescence (PL) spectroscopy, atomic force microscopy (AFM), and field-emission scanning electron microscopy (FE-SEM). The thickness of each prepared thin film was obtained by Fizeau interference fringes[31–33] that required a He-Ne laser source and a beam expander. Thin film thickness was calculated as[31]

$$t = 316.4\,\Delta x/x \ \text{(nm)}, \tag{1}$$

where x is the width of the bright fringe and Δx is the spacing between two consecutive fringes resulting from destructive interference.

The crystallite size of the predominant peaks was calculated by Scherrer's equation[34,35]:

$$\mathrm{D} = \mathrm{K}\lambda/\beta * \cos(\theta)\,\text{(nm)}, \tag{2}$$

where D is the crystallite size, K is a constant (0.94), λ is the exciting x-ray wavelength, β is the full width at half maximum (FWHM), and θ is the half angle position between the incident and the scattered wavelength.

The dislocation density values were also calculated by[36,37]

$$= 1/\mathrm{D}^2(line.m^{-2}), \tag{3}$$

where δ is the dislocation density and D is the crystallite size (nm).

The microstrain of the prepared films was calculated by Wilson's formula[38,39]:

$$\varepsilon = \beta/4\tan\theta * 10^3, \tag{4}$$

where ε is the microstrain, β is the full width at half maximum (radians), and θ is half the diffraction angle position (radians).

From the UV–Vis data, the optical absorption coefficients as a function of the excitation ratio were calculated by using the following equation[40,41]:

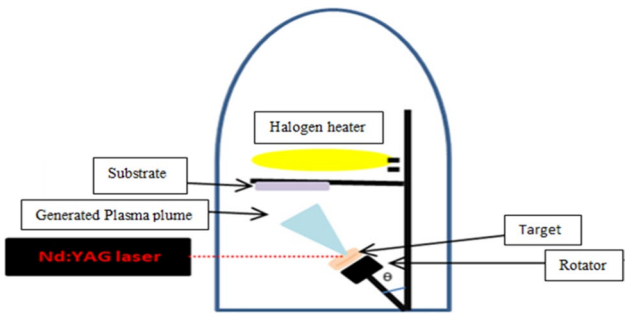

Fig. 1 Pulsed laser deposition system.

$$\alpha = 2.303\mathrm{At}\ (\mathrm{cm}^{-1}), \tag{5}$$

where α is the absorption coefficient, A is the absorption percentage, and t is the thin film thickness.

The incident photon energy was calculated by[42,43]

$$\mathrm{Eg}\ (\mathrm{eV}) = 1240\ (\mathrm{nm.eV})\lambda\ (\mathrm{nm}). \tag{6}$$

The optical bandgap values were obtained by Tauc's equation[44–46]:

$$(\alpha h\nu) = B(h\nu - Eg)^1/r, \tag{7}$$

where h is the Planck constant, ν is the frequency of the incident photon, B is a constant that is the band tailing parameter, and r is a constant with different values based on the material type transitions.

Results and Discussion

The thickness values of the prepared thin films, shown in Fig. 2, increased as the laser fluence increased. When the laser fluence exceeds the ablation threshold of the target, the absorption of laser energy is higher and more evaporation occurs, leading to the availability of more species in each laser pulse,[47] and hence more layers obtained. The linear relationship between film thickness and laser energy fluence provides a basis for a precise and efficient deposition of numerous film layers. This relationship is instrumental in improving the material used, improving the device performance, and increasing production processes, making it an important advantage in the research field and industrial applications. The ability to correlate the thickness of a thin film linearly with laser fluence (amount of energy falling per unit area) in thin film deposition processes such as PLD has several benefits. For example, the potential for scaling enables accurate control of the thickness through the use of fluence, and the prediction of thickness via the linear relationship makes the process highly predictable. In addition, thin films with controlled thickness have consistent optical, electrical, and mechanical properties, which are important for high-performance devices because they help in reducing variations between different production runs and help to ensure similar characteristics among films in the same batch with adequate reproducibility.

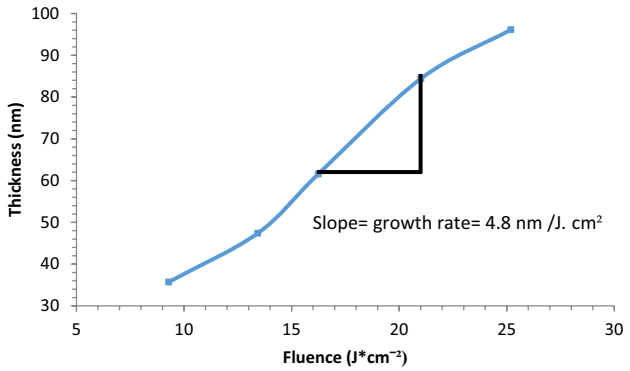

Fig. 2 Thin film thickness as a function of laser fluence.

In thin film deposition methods including PLD, the gradient of the plot of film thickness versus laser fluence refers to the deposition rate with respect to the unit of laser fluence. It offers essential information on the material deposition efficiency in converting laser energy into materials on the substrate. The results show a slope of about 4.8 nm/J cm^2, where the steepness of the slope refers to the thin film growth, which is affected by the laser. This means that a slight increase in laser fluence results in a greater increase in film thickness, implying that the deposition efficiency is higher. The slope explains how the laser interacts with the material being targeted, and properties such as absorption, thermal conductivity, and material evaporation thresholds determine how well laser energy is utilized. A steeper slope means that the energy of the laser is absorbed and translated into the process of deposition, which results in thicker film per unit increase in fluence.

An x-ray diffractometer (XRD-6000, Shimadzu) with a Cu-Kα radiation source at a wavelength of 0.15406 nm was employed to investigate the diffraction patterns of the prepared films. Each sample was scanned in the 2θ range from 20° to 60°.

The XRD profile demonstrated the formation of Nb_2O_5 thin films with increasing laser fluence as shown in Fig. 3. At 9.3, 13.4, and 16.2 J/cm^2 laser fluence, the deposited films showed very weak patterns. This is due to low kinetic energy, and hence low species velocity, causing the plume particles to collide randomly and expand away from the target–substrate normal direction. As a result, a low number of particles are deposited on the substrate surface. This phenomenon mainly depends on the target material ionization energy and the laser wavelength employed.[48] At 21 J cm^{-2}, T-Nb_2O_5 (orthorhombic) and H-Nb_2O_5 (monoclinic) structures were formed with well-defined peaks as shown in Fig. 4. The angle positions (2θ) of the observed polycrystalline peaks were centered at 22.6°, 26.1°, 28.8°, 35.4°, and 36.9°, with related Miller indices assigned to (0 0 1), (4 0 2), (2 0 0), (3 1 3), and (2 0 1) planes, respectively. The obtained diffraction planes and their Miller indices were based on JCPDS card nos. 00-030-0873 and 00-009-0372, respectively. The (200) plane was the predominant plane. The intense sharp peak of this plane was due to the enhanced crystallization and the better stacking of the film layers. However, a further increase in the laser fluence showed a decrease in the peak intensity obtained at the (2 0 0) diffraction plane. Higher energy density per laser pulse

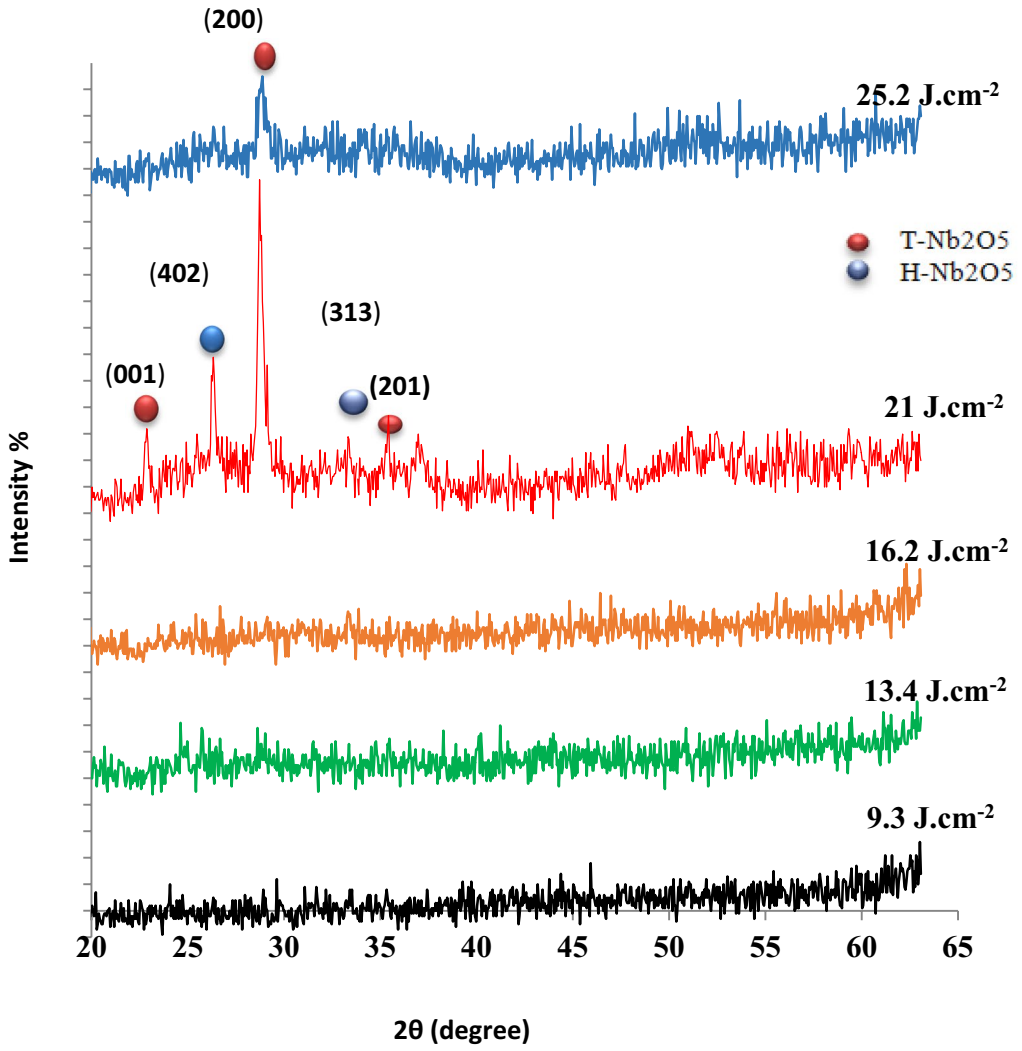

Fig. 3 XRD data of Nb_2O_5 films prepared at different laser fluence.

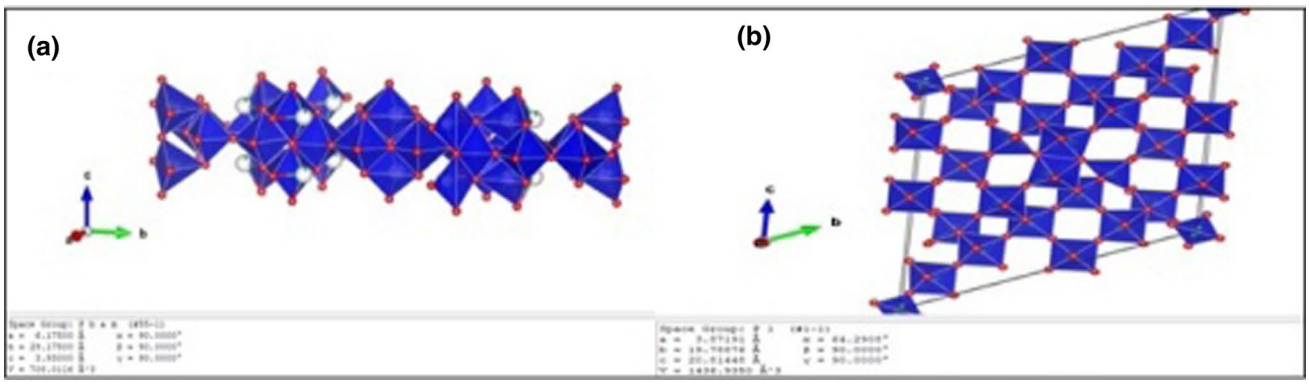

Fig. 4 (a) T-Nb_2O_5 phase structure. (b) H-Nb_2O_5 phase structure.

induces more thermal shockwaves. These shockwaves cause a mechanical impact on the target surface, hence influencing the ablated species. During the deposition process, higher ejection of the target surface was clearly observed at 25.2 J cm^{-2} in comparison with lower fluence. In addition to the reasons mentioned above, large droplet formation or poorly

stacked deposited layers due to experimental or physical conditions may explain the lower intensity observed for the film deposited at 25.2 J cm^{-2}.[48,49]

Important calculations for the obtained planes including FWHM, grain size, dislocation density, and microstrain are provided in Table I. The FWHM values for the Nb_2O_5 film deposited at 21 J cm^{-2} and 25.2 J cm^{-2} are influenced by the laser energy, which generally causes a considerable change in the ejected flux.[50] It is also impacted by thermal stress that arises from anisotropic lattice expansion as well as microstrain or other defects.[51,52]

Other parameters including the d-spacing, lattice constants, and related phases are listed in Table II.

Based on Scherrer's equation, the grain size is inversely proportional to the FWHM. The widest peak is associated with the smallest crystallite size. It can be observed that the crystallite size of the (2 0 0) plane obtained by 21 J cm^{-2} is higher than the crystallite size obtained by 25.2 J cm^{-2}. In addition, the higher crystallite size for 21 J cm^{-2} caused lower dislocation density at the predominant (2 0 0) plane as compared with 25.2 J cm^{-2}. In addition to the XRD profile, Raman spectroscopy is an important nondestructive technique for characterizing the film structure. The Raman spectra of the sample identify the film structure by interacting with the vibrational modes of the film molecules and depend primarily on the polarizability.

The prepared thin films were tested using Raman spectroscopy (Sunshine V2-86 spectrometer). As shown in Fig. 5, the intense peaks observed below 400.6 cm^{-1} are attributed to the bending modes of NbO_6 octahedra, while those around 600 cm^{-1} are related to stretching modes; a similar range was obtained by Joya et al.[53] The bands that exceeded 1000 cm^{-1} were attributed to edge-shared octahedra. The band located at 642.3 cm^{-1} was obtained from T-Nb_2O_5 for the film prepared at 21 J cm^{-1}, and an approximate indication was found by Guan et al.[54] For the thin film prepared at 25.2 J cm^{-1}, the T-Nb_2O_5 band was assigned at 611 cm^{-1}. At 990.2 cm^{-1}, an intense H-Nb_2O_5 broadened band was observed.[55–57] Other weak bands emerged at approximately 460.1 cm,$^{-1}$ indicating the framework vibration of oxygen. A very approximate indication was found by Palatnikov et al.[58] Molecular bands observed for thin films prepared at laser fluence of less than 21 J cm^{-2} showed values shifted to lower frequencies, indicating the octahedral distortion of the weak patterns.

The broadening in Raman spectra can be attributed to the phonon line width modes as a function of temperature, along with other parameters including thermal expansion and strain induced by lattice mismatch. Observations of broadening were also reported by Wang et al.[59] It can be observed that bands below 400.6 cm^{-1} showed higher intensity with increasing laser fluence. This may be an indication of the compression of the material that exhibits disorders. This kind of compression leads to increased intensity and a slight decrease in the line width. This behavior was similarly found by Joya et al.[53] and Fakhri et al.[60] The values obtained were shifted to longer or lower wavenumbers in comparison with those reported by Palatnikov et al.,[58] Wang et al.,[59] and Khashan et al.,[61] due to different preparation methods and the compression or decompression of the material molecules. In order to optimize Raman line width to improve the material properties, the line width must be reduced, which includes improving the resolution and sensitivity of Raman spectroscopic measurements. Lower line widths mean good-quality and well-crystallized materials, resulting in finer details in vibrational modes in these materials. There are different methods to obtain this such as the use of high-purity starting raw materials to minimize impurities and defects, which aids in broadening the Raman line width. In addition, defects can be reduced and crystal quality enhanced by post-synthesis thermal annealing, leading to

Table I XRD calculations for the predominant films at 21 J cm^{-2} and 25.2 cm^{-2}.

Fluence (J cm^{-2})	2θ (°)	FWHM (°)	D (nm)	δ*10^3	ε*10^3
21	22.6	0.2952	27.56	1.31	0.40
	26.1	0.1961	41.07	0.59	0.50
	28.8	0.2460	71.76	0.93	0.39
	35.4	0.2514	31.45	1.01	0.55
	36.9	0.3804	20.70	2.33	0.29
25.2	28.7	0.3936	20.43	2.39	0.43

Table II d-Spacing, Miller indices, and structural phases obtained at 21 and 25 J cm^{-2}

Fluence (J cm^{-2})	2θ (°)	d-spacing (Å)	Miller indices (*hkl*)	Lattice constants (Å)	Structural phase
21	22.6	3.88	0 0 1	a = 6.17, b = 29.17, c = 3.93	T-Nb_2O_5
	26.1	3.38	4 0 2	a = 21.34, b = 3.81, c = 19.47	H-Nb_2O_5
	28.8	3.10	2 0 0	a = 6.17, b = 29.17, c = 3.93	T-Nb_2O_5
	35.4	2.54	3 1 3	a = 21.34, b = 3.81, c = 19.47	H-Nb_2O_5
	36.9	2.42	2 0 1	a = 6.17, b = 29.17, c = 3.93	T-Nb_2O_5
25.2	28.7	3.12	2 0 0	a = 6.17, b = 29.17, c = 3.93	T-Nb_2O_5

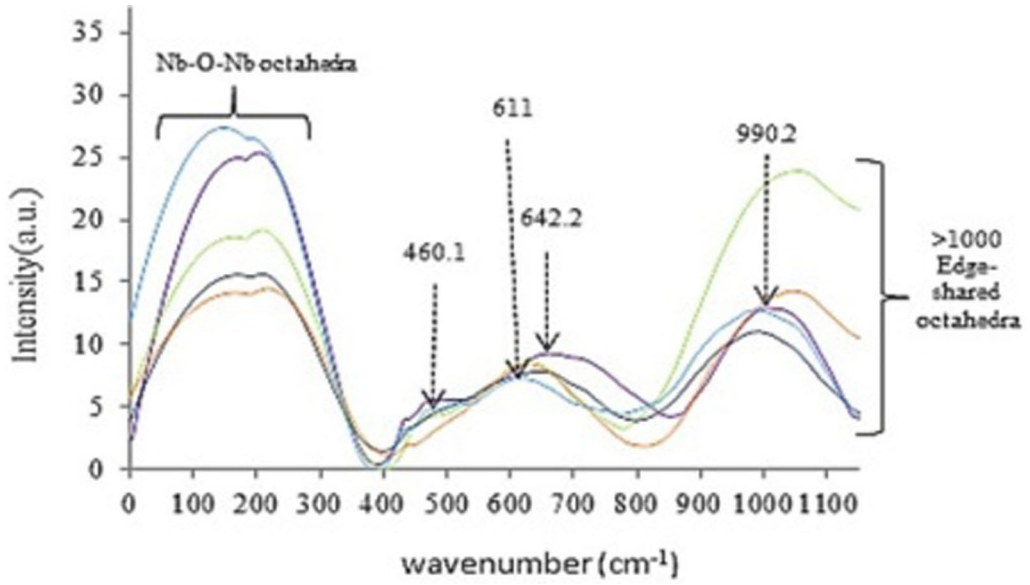

Fig. 5 Raman spectra of prepared Nb_2O_5 thin films.

narrower Raman peaks. The optimum temperature and time for annealing must suit each individual material.

A double-beam UV–Vis spectrophotometer (Shimadzu UV-1800) was used to obtain the transmission and absorption of each prepared film. It can be observed in Fig. 6 that the transmission decreased with increasing laser fluence. The decreased transmission may indicate the deposition of larger particles as the laser energy density increased. It may also indicate the organized and well-formed layers that were achieved during the deposition process. The absorbance of all films, as shown in Fig. 7, was in the UV region of the spectrum, attributed to the intrinsic semiconductor crystals. In this study, indirect bandgaps were estimated. The indirect bandgap energy values were calculated by Tauc's plot, shown in Fig. 7, resulting in more approximate bandgap values with PL analyses.

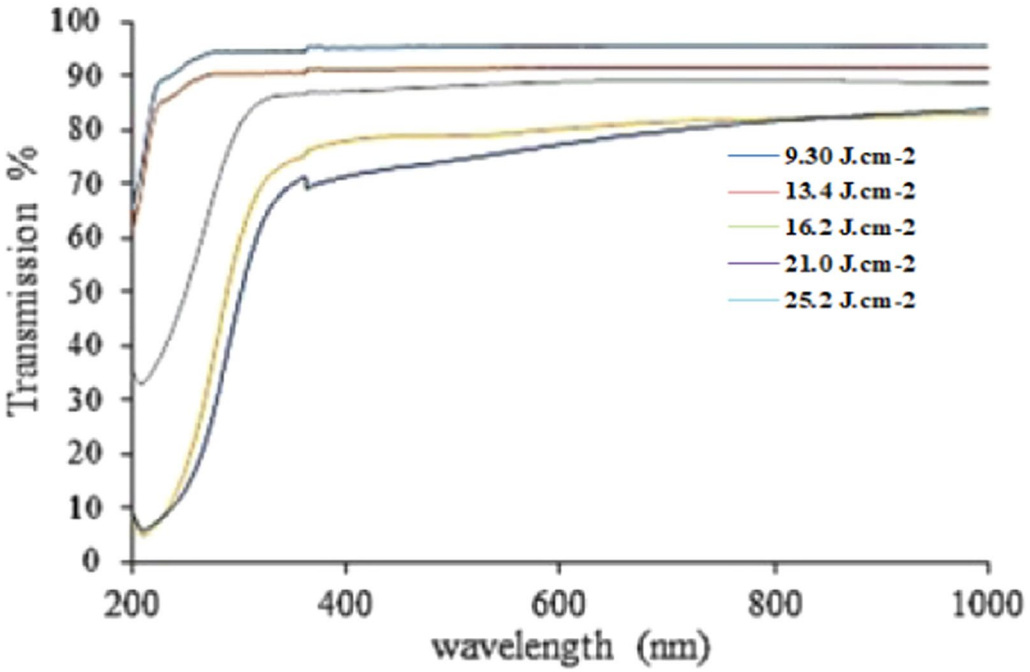

Fig. 6 Transmission spectra of synthesized Nb_2O_5 thin films as a function of wavelength range at different fluence values.

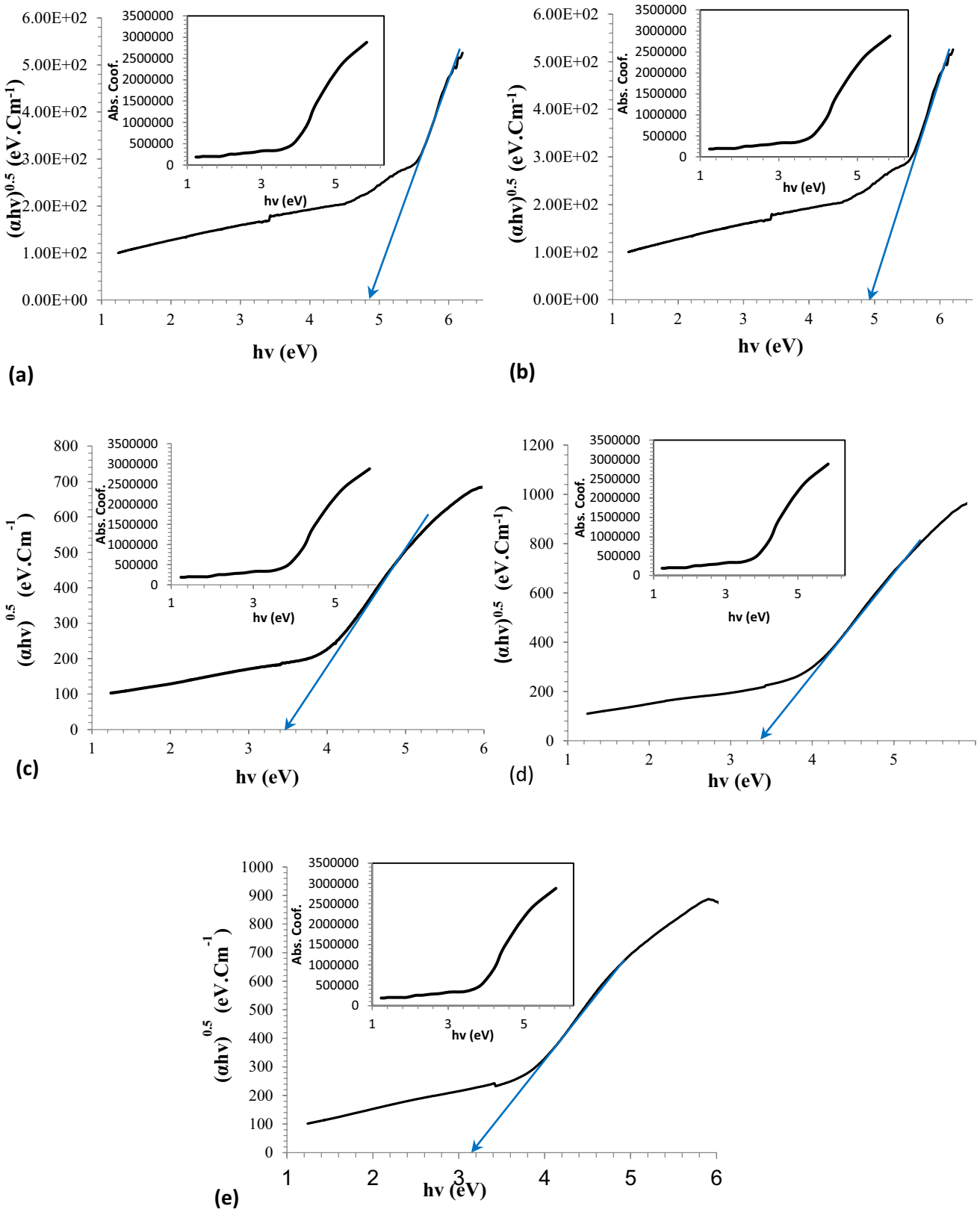

Fig. 7 Tauc plot estimations of the bandgaps of the films prepared at (a) 9.3 J cm^{-2}, (b) 13.4 J cm^{-2}, (c) 16.2 J cm^{-2}, (d) 21 J cm^{-2}, and (e) 25.2 J cm^{-2}.

The energy gap is the most important parameter, since it indicates the thin film behavior and potential for use in applications such as solar cells or detectors. Estimated bandgap energy values of 4.81 eV, 4.73 eV, 3.41 eV, 3.29 eV, and 3.21 eV, respectively, were determined for the thin films. As the laser energy density increased, the absorbance of the prepared films also increased. This increase led to higher excitation from the valence band to the conduction band, which affected the obtained bandgap values showing a reduction trend. Increasing laser fluence might lead to the formation of tiny nanoparticles due to the efficient ablation process. In the case of materials where quantum confinement effects are considerable, smaller nanoparticles typically show larger bandgaps. If the increased laser fluence leads to larger or aggregated particles due to the elevated temperatures and long growth times, the bandgap may decrease. In addition, increased laser power can improve the surface states of nanoparticles, which can interact with the bulk states and effectively reduce the bandgap. Therefore, proper tuning of laser fluence through a detailed characterization enhances the properties and desired electronic characteristics of thin films or nanomaterials for the specific application.

The PL spectra indicated that emission began at 351 nm, with 330 nm as an excitation wavelength. In Fig. 8, UV emission and other peaks in the given spectra can be observed. The emission peak at 367 nm (3.37 eV) was due to the near-band-edge (NBE) emission that occurs from the conduction band minimum to the valence band maximum. Higher and lower peaks were shifted to longer wavelengths at 373 nm and 401 nm, respectively. The peak observed at 401 nm related to the bandgap of about 3.09 eV, while the estimated bandgap of 2.6 eV was related to 474 nm. The observed peaks at 538 nm and 560 nm were related to 2.3 eV and 2.21 eV, respectively. Other observations were at 560 nm, 624 nm, and 651 nm due to the inner optical gap transitions resulting from defects or oxygen vacancies, or even associated with NbO_6 octahedral distortion.

Emissions at 367 nm and 560 nm were reported by Fakhri et al.[62] and Xu,[63] respectively. However, other values were in approximate agreement with the same emission range found by Ismail et al.[64] and Boruah et al.,[65] with some higher or lower values due to different deposition routes. The broadened peaks may indicate that the phonons add momentum in the indirect transition process. The obtained PL bandgaps are in agreement with the bandgaps estimated by Tauc's plot, with slightly higher or lower values that are normal in PL analyses.[66,67] When analyzing the emission spectrum, PL results give a clear view of defects present inside material samples. The type of defects present, their concentrations, and the optical properties of the material can be distinguished by observing the emission peak placement or width as well as how much they stand out from others (intensity) on their own. This may be important in some uses such as optoelectronics because we require particular properties of diodes and photocatalysts that have been perfectly tailored with respect to their defects. Potential material defects include vacancies, interstitials, antisites, dislocations, or impurities (dopants). These defects cause separate energy

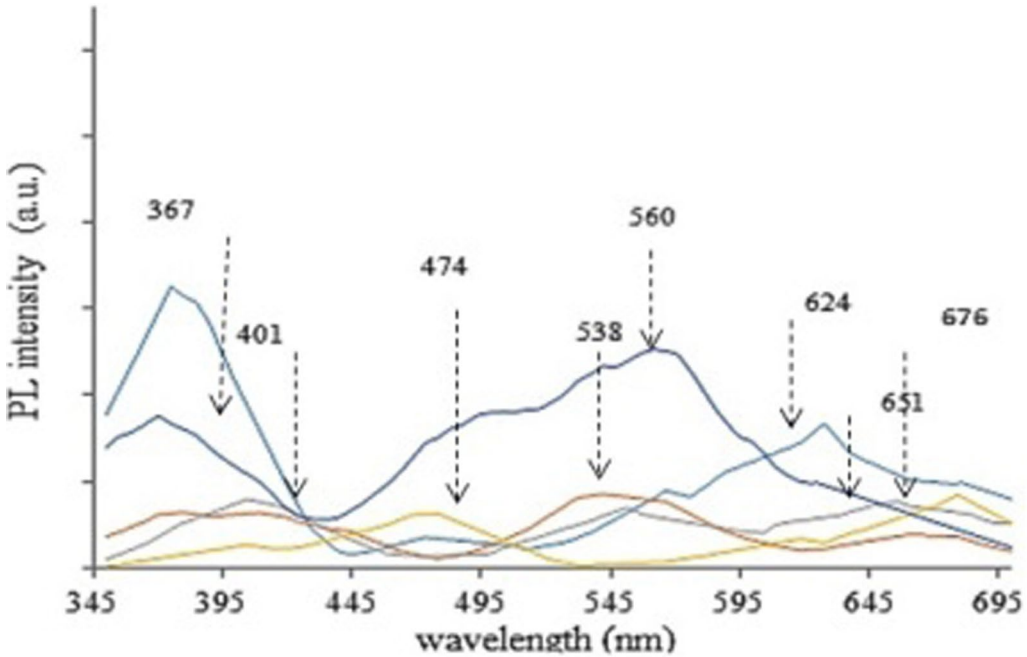

Fig. 8 PL spectra at different laser fluence values.

levels to form within the bandwidth area, some of which may serve as emission or radiation centers while others may quench only to give off heat. Recombination involving electron–hole pairing across the forbidden band gives rise to peaks around the position of the band edge in PL spectra.

The presence of defects is shown by peaks at energy levels that are lower than the band edge. Emissions which are caused by levels of defects undergoing transition result in peaks. There are often problems such as voids and interstitials associated with deep defects which correspond to deep-level emissions that are emitted at wavelengths far below the conduction band edge. Differences in peripheral locations may be an indicator of alterations in either the amount or kind of defects.

Thin film roughness and topographic measurements were investigated by AFM. As the laser fluence increased, the surface average and root-mean-square (RMS) roughness values also increased. The correlation between the laser energy density and the surface roughness is clarified in Table III. Prepared film topographies are shown in Fig. 9. Obviously, the laser energy density impacted the surface roughness that was comparable with thickness. However, the smoothest surface belonged to the film prepared at 21 J cm^{-2}. At this energy density, as shown in the XRD profile, well-defined planes were observed and the deposited particles were somewhat merged within the surface.

FE-SEM results provided the surface morphology of each prepared film as shown in Fig. 10a–e.

One drawback of the PLD technique is the droplet formation on the target's surface due to the mechanical force exposure. Increasing laser energy density causes an increase in the observed particle size.[68,69] The obtained films showed a relative reduction in droplet formation as the laser energy density increased. The film deposited at 21 J cm^{-2} showed the smallest droplets, the most homogeneous structure, and a morphological enhancement. At the lowest selected laser fluence, 9.3 J cm^{-2}, the prepared film morphology showed very small particles with spherical clusters that were randomly distributed. With an increase in the laser energy density to 13.4 J cm^{-2} (Fig. 10b), cauliflower-like structures were observed. Higher laser fluence (Fig. 10c–e) revealed the formation of films with different particle sizes and some droplets. Energy-dispersive x-ray analysis (EDX), shown in Fig. 11a–e, provides the elemental composition and allows us to estimate the stoichiometric values of the prepared Nb_2O_5 films.

As the laser energy density increased, the prepared films showed a higher niobium-to-oxygen ratio, indicating enhanced crystallization.[70,71] The data obtained from the EDX analyses are listed in Table IV.

The thin film prepared at 21 J cm^{-2} provided the highest Nb and O content percentages as well as the highest stoichiometry. These results were confirmed by the XRD profile.

Table III Root-mean-square and average roughness for each prepared film at different laser fluence values

Fluence (J cm⁻2)	RMS roughness (nm)	Average roughness (nm)
9.3	0.95	0.72
13.4	3.32	2.17
16.2	4.06	2.97
21	1.57	1.26
25.2	4.27	2.81

Conclusion

The results of this study showed that the prepared thin films became thicker as the laser beam increased. As film thickness varies directly with the amount of laser power, precise and cost-effective material deposition can be achieved. In particular, the deposition rate and growth of the thin films depended on the steepness of the slope of their thickness plotted against laser fluence. The Nb_2O_5 thin films were formed as revealed by XRD analysis. However, when the laser fluence was varied, changes in their crystal structure were observed. Consequently, it was necessary to calculate parameters relating to each order of diffraction peak for precise numbers regarding the grain size, dislocation density, and microstrain of these films via XRD data. Furthermore, information concerning their structure and the presence of different vibrational modes was obtained from Raman spectroscopy measurements. The findings showed that as the laser fluence increased, absorbance increased while transmission decreased according to UV–Vis spectroscopy. The indirect bandgap values of the films were estimated using Tauc's plot. Different emission wavelengths were observed in the PL spectra, indicating some defects within these films. AFM revealed an increase in the surface roughness on many of the films as laser fluence was increased, and EDX analysis confirmed that the films retained the same ratio of precursor elements.

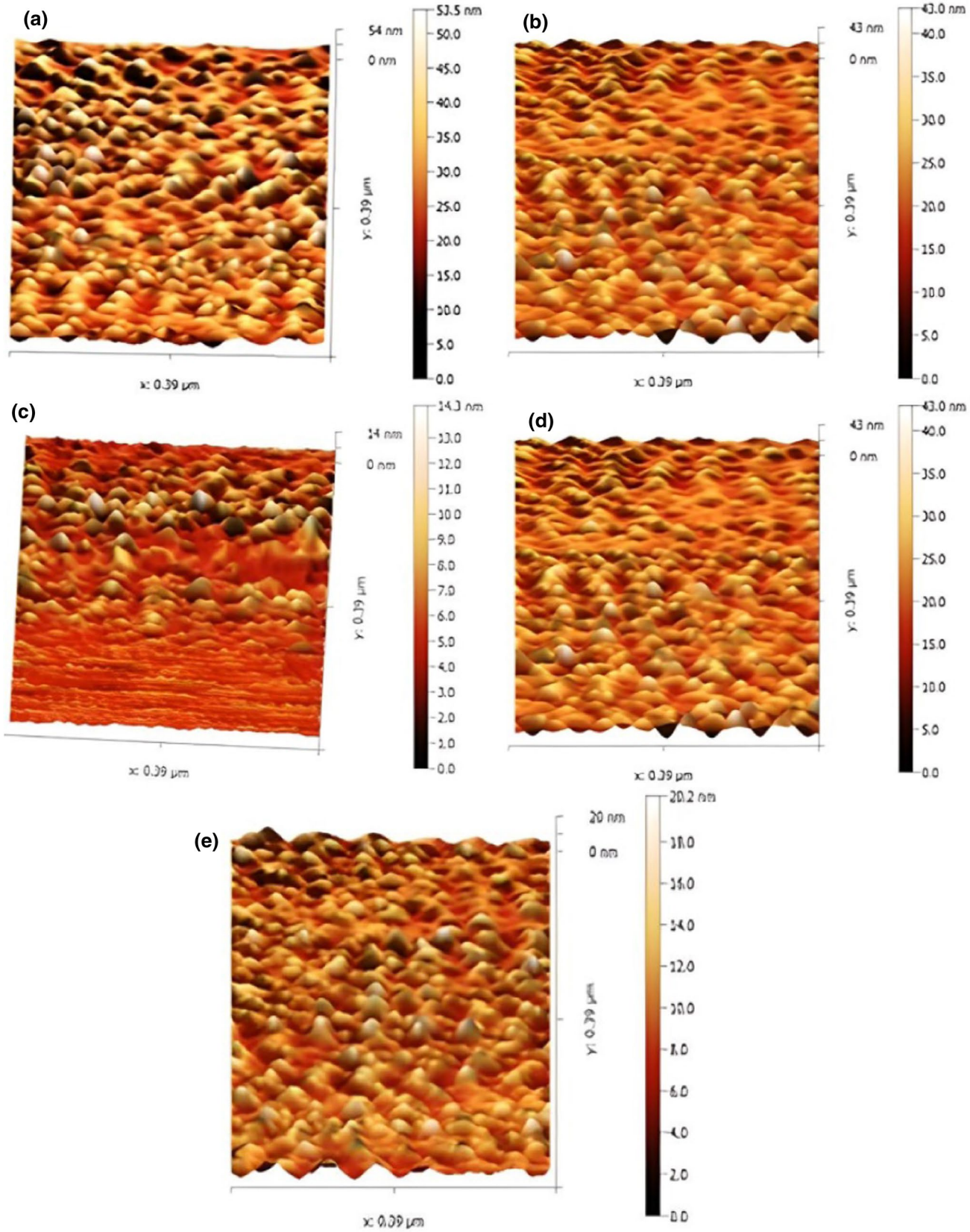

Fig. 9 Surface topography and histograms of the films obtained at (a) 9.3 J cm^{-2}, (b) 13.4 J cm^{-2}, (c) 16.2 J cm^{-2}, (d) 21 J cm^{-2}, and (e) 25.2 J cm^{-2}.

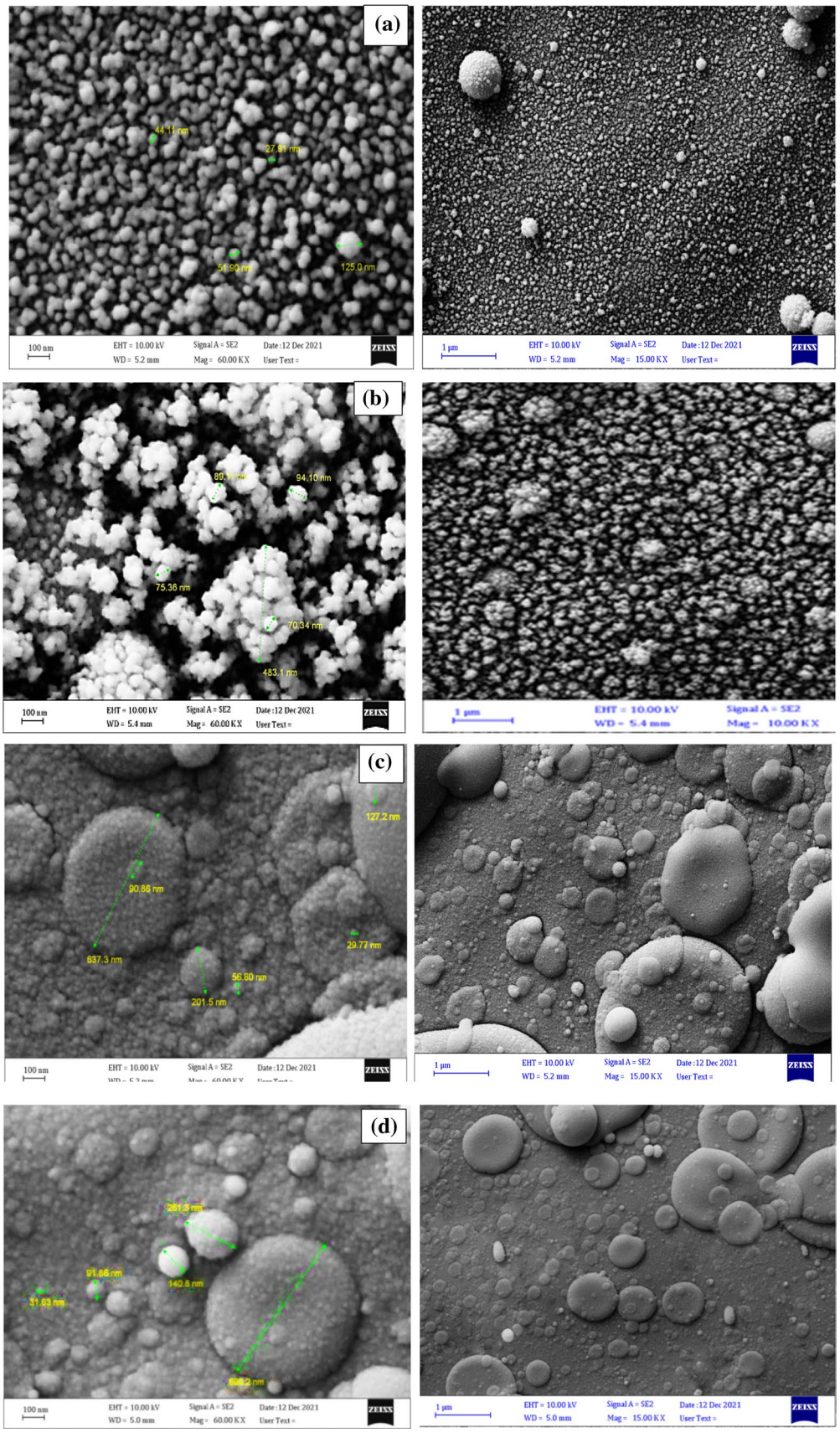

Fig. 10 FE-SEM of thin films with 100 nm and 1 µm scales at (a) 9.3 J cm^{-2}, (b)13.4 J cm^{-2}, (c) 16.2 J cm^{-2}, (d) 21 J cm^{-2}, and (e) 25.2 J cm^{-2}.

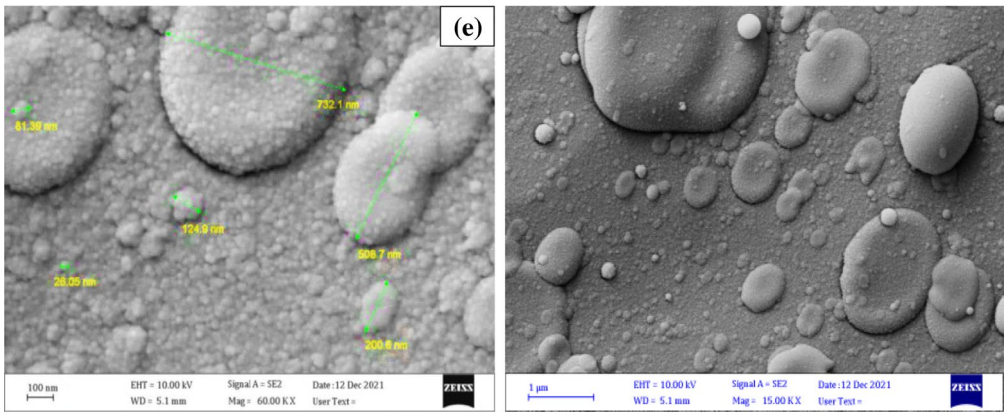

Fig. 10 (continued)

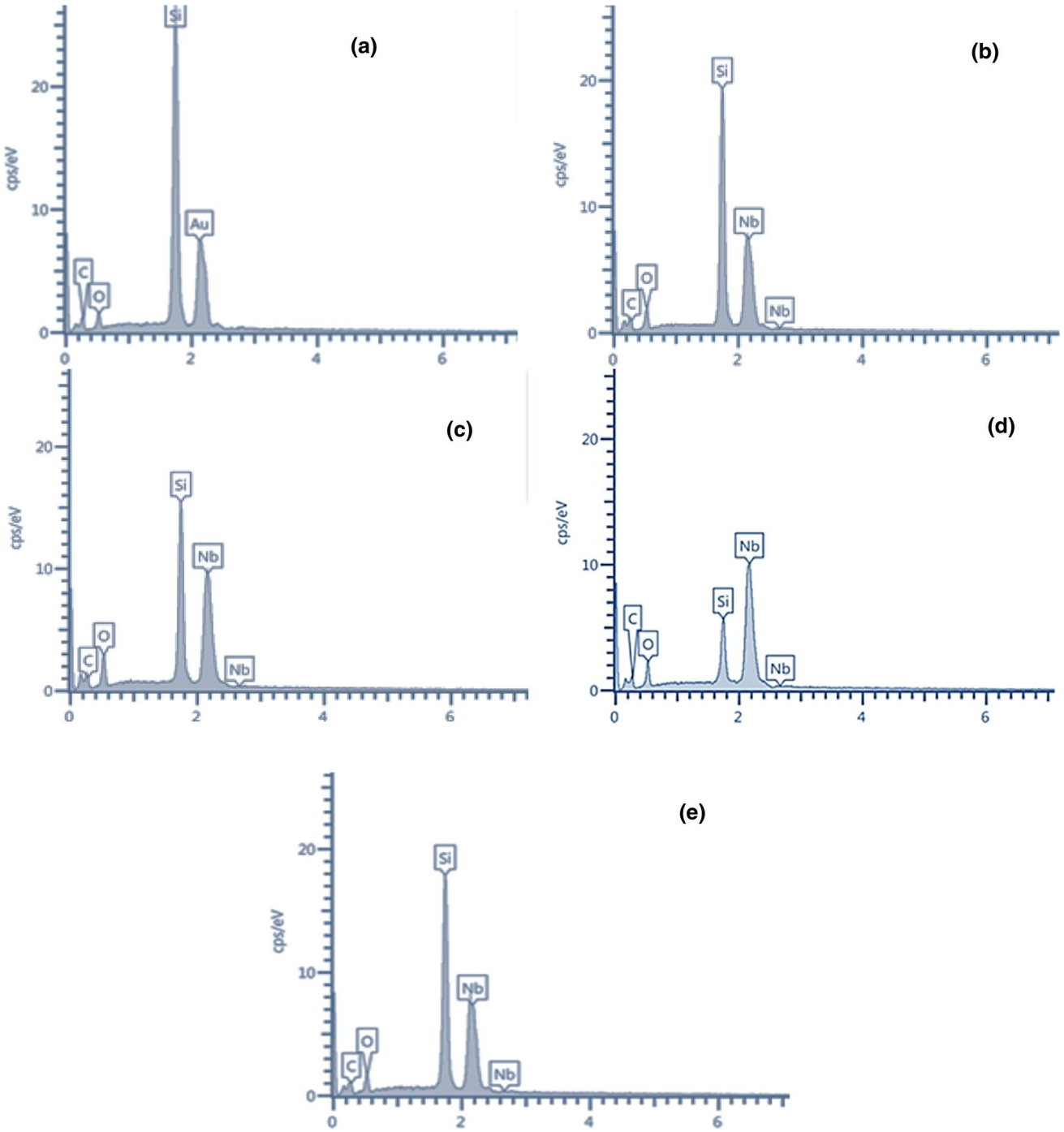

Fig. 11 EDX analyses illustrating elemental composition for (a) 9.3 J cm^{-2}, (b)13.4 J cm^{-2}, (c) 16.2 J cm^{-2}, (d) 21 J cm^{-2}, and (e) 25.2 J cm^{-2}.

Table IV EDX analysis of Nb and O for different laser fluence values

Fluence (J cm^{-2})	Nb wt.%	O wt.%	Nb (σ)	O (σ)	Nb/O	Si atomic %	Nb atomic %	O atomic %	C atomic %
9.3	–	–	–	–	–	52.3	34.6	11.7	1.4
13.4	13.5	4.4	1.2	0.3	3.1	41.8	44.5	12.6	1.1
16.2	25.1	5.6	1.5	0.4	4.5	35.4	49.7	14.1	0.8
21	66.1	8.8	1.2	0.5	7.5	29.6	53.8	15.9	0.7
25.2	45.7	8.1	2.5	0.4	5.6	40.5	46.2	12.4	0.9

Acknowledgments The authors would like to thank the University of Technology-Iraq for the logistic support for this work. The authors extend their appreciation to the Deanship of Scientific Research at Northern Border University, Arar, KSA, for the logistic support for this work. The authors extend their appreciation to the Deanship of Scientific Research at Northern Border University, Arar, KSA, for funding this research work through the project number NBU-FFR-2024-1299-08. The authors would like to thank Al-Mustaqbal University College, Department of Medical Physics, Iraq, for the logistic support for this work. The authors would like to thank Warith Al-Anbiyaa University, Karbala, Iraq, for the logistic support for this work.

Authors' Contributions Conceptualization: Evan T. Salim, Mohammed Jalal AbdulRazzaq, Makram A. Fakhri. Methodology: Evan T. Salim, Suhair R. Shafeeq, Mohammed Jalal AbdulRazzaq, Makram A. Fakhri. Software: Evan T. Salim, Suhair R. Shafeeq, Mohammed Jalal AbdulRazzaq, Makram A. Fakhri, Ahmad S. Azzahrani, Ali Basem, Forat H. Alsultany, Subash C.B. Gopinath. Validation: Evan T. Salim, Suhair R. Shafeeq, Mohammed Jalal AbdulRazzaq, Makram A. Fakhri, Ahmad S. Azzahrani, Ali Basem, Forat H. Alsultany, Subash C.B. Gopinath. Formal analysis: Evan T. Salim, Suhair R. Shafeeq, Mohammed Jalal AbdulRazzaq, Makram A. Fakhri, Ahmad S. Azzahrani, Ali Basem, Forat H. Alsultany, Subash C.B. Gopinath. Investigation: Evan T. Salim, Suhair R. Shafeeq, Mohammed Jalal AbdulRazzaq, Makram A. Fakhri, Ahmad S. Azzahrani, Ali Basem, Forat H. Alsultany, Subash C.B. Gopinath. Resources: Evan T. Salim, Suhair R. Shafeeq, Mohammed Jalal AbdulRazzaq, Makram A. Fakhri, Ahmad S. Azzahrani, Ali Basem, Forat H. Alsultany, Subash C.B. Gopinath. Data curation: Evan T. Salim, Suhair R. Shafeeq, Mohammed Jalal AbdulRazzaq, Makram A. Fakhri, Ahmad S. Azzahrani. Writing—original draft preparation: Suhair R. Shafeeq. Writing—review and editing: Evan T. Salim, Mohammed Jalal AbdulRazzaq, Makram A. Fakhri, Ahmad S. Azzahrani, Ali Basem, Forat H. Alsultany, Subash C.B. Gopinath. Visualization: Evan T. Salim, Suhair R. Shafeeq, Mohammed Jalal AbdulRazzaq, Makram A. Fakhri, Ahmad S. Azzahrani, Ali Basem, Forat H. Alsultany, Subash C.B. Gopinath. Supervision: Evan T. Salim, Mohammed Jalal AbdulRazzaq. Project administration: Evan T. Salim, Mohammed Jalal AbdulRazzaq, Makram A. Fakhri. Funding acquisition: None. All authors have read and agreed to the final version of the manuscript.

Funding The study detailed in this manuscript was supported by Northern Border University, Arar, KSA, for funding this research work through the project number NBU-FFR-2024-1299-08'.

Data Availability Correspondence and requests for materials should be addressed to Makram A. Fakhri, Suhair R. Shafeeq, and Evan T. Salim.

Declarations

Conflict of interest This statement serves as an official confirmation that the authors involved in this paper do not possess any conflicts of interest. Furthermore, we assert that the disclosure provided in relation to this publication is comprehensive and accurate, based on the most reliable information available to us. We concur that in the event that we acquire any knowledge suggesting the potential inaccuracy of this declaration or non-compliance with the conflict of interest policy, we will promptly tell the journal.

Ethics approval Not applicable.

Consent to participate Not applicable.

Consent for publication Not applicable.

References

1. H. Luo, W. Song, P.G. Hoertz, K. Hanson, R. Ghosh, S. Rangan, M.K. Brennaman, J.J. Concepcion, R.A. Binstead, R.A. Bartynski, and R. Lopez, A sensitized Nb_2O_5 photoanode for hydrogen production in a dye-sensitized photoelectrosynthesis cell. *Chem. Mater.* 25(2), 122 (2013).
2. N.C. Emeka, P.E. Imoisili, and T.C. Jen, Preparation and characterization of Nb x O y thin films: a review. *Coatings* 10(12), 1246 (2020). https://doi.org/10.3390/coatings10121246.
3. S.R. Shafeeq, M.J.A. Razzaq, E.T. Salim, and M.H.A. Wahid, Significance of niobium (V) oxide for practical applications: a review. *Key Eng. Mater.* 911, 89 (2022).
4. I. Nowak, and M. Ziolek, Niobium compounds: preparation, characterization, and application in heterogeneous catalysis. *Chem. Rev.* 99(12), 3603 (1999).
5. M.K. Abood, E.T. Salim, J.A. Saimon, and A.A. Hadi, Electrical conductivity, mobility and carrier concentration in Nb_2O_5 films: effect of NH_4OH molarity. *Int. J. Nanoelectron. Mater.* 14(3), 259 (2021).
6. K.T. Jacob, C. Shekhar, M. Vinay, and Y. Waseda, Thermodynamic properties of niobium oxides. *J. Chem. Eng. Data* 55(11), 4854 (2010).
7. M.A. Fakhri, Y. Al-Douri, E.T. Salim, U. Hashim, Y. Yusof, E.B. Choo, Z.T. Salim, and Y.N. Jurn, Structural properties and surface morphology analysis of nanophotonic LINBO3. *ARPN J. Eng. Appl. Sci.* 11(8), 4974 (2016).
8. M.A. Aegerter, Sol–gel niobium pentoxide: a promising material for electrochromic coatings, batteries, nanocrystalline solar cells and catalysis. *Sol. Energy Mater. Sol. Cells* 68(3–4), 401 (2001).
9. R.A. Ismail, E.T. Salim, and H.T. Halbos, Preparation of Nb_2O_5 nanoflakes by hydrothermal route for photodetection applications: the role of deposition time. *Optik* 245, 167778 (2021).

10. G. RobáLee, Electrochromic Nb_2O_5 and Nb_2O_5/silicone composite thin films prepared by sol–gel processing. *J. Mater. Chem.* 1(3), 381 (1991).
11. M.A. Fakhri, R.A. Ismail, A.K. Abass, L.Z. Mohammed, F.H. Alsultany, and U. Hashim, Synthesis of $LiNbO_3/SiO_2/Si$ nanostructures layer by layer based on Mach–Zehnder modulator using pulsed laser deposition route. *SILICON* 14, 11781 (2022). https://doi.org/10.1007/s12633-022-01902-5.
12. K. Xu, Integrated silicon directly modulated light source using p-well in standard CMOS technology. *IEEE Sensors J.* 16(16), 6184 (2016). https://doi.org/10.1109/JSEN.2016.2582840.
13. E.T. Salim, R.A. Ismail, and H.T. Halbos, Deposition geometry effect on structural, morphological and optical properties of Nb_2O_5 nanostructure prepared by hydrothermal technique. *Appl. Phys. A* 126, 891 (2020).
14. S. George, and M.T. Sebastian, Synthesis and microwave dielectric properties of novel temperature stable high Q, $Li_2ATi_3O_8$ (A = Mg, Zn) ceramics. *J. Am. Ceram. Soc.* 93(8), 2164 (2010). https://doi.org/10.1111/j.1551-2916.2010.03703.xcouldbementioned.
15. E.T. Salim, J.A. Saimon, M.K. Abood, and M.A. Fakhri, Effect of silicon substrate type on Nb_2O_5/Si device performance: an answer depends on physical analysis. *Opt. Quant. Electron.* 52(10), 463 (2020).
16. M.K. Hota, M.K. Bera, S. Verma, and C.K. Maiti, Studies on switching mechanisms in Pd-nanodot embedded Nb_2O_5 memristors using scanning tunneling microscopy. *Thin Solid Films* 520(21), 6648 (2012).
17. L.Z. Mohammed, M.A. Fakhri, and A.K. Abass, Structural and optical properties of nanostructured hybrid $LiNbO_3$/silicon wafer for fabricating optical modulator. *J. Phys. Conf. Ser.* 1795(1), 012055 (2021).
18. R.A. Rani, A.S. Zoolfakar, A.P. O'Mullane, M.W. Austin, and K. Kalantar-Zadeh, Thin films and nanostructures of niobium pentoxide: fundamental properties, synthesis methods and applications. *J. Mater. Chem. A* 2(38), 15683 (2014). https://doi.org/10.1039/c4ta02561j.
19. C.-S. Lee, D. Kwon, J.E. Yoo, B.G. Lee, J. Choi, and B.H. Chung, A highly sensitive enzyme-amplified immunosensor based on a nanoporous niobium oxide (Nb_2O_5) electrode. *Sensors* 10(5), 5160 (2010).
20. V.C.B. Leitune, F.M. Collares, A. Takimi, G. Brito de Lima, C.L. Petzhold, C.P. Bergmann, and S.M.W. Samuel, Niobium pentoxide as a novel filler for dental adhesive resin. *J. Dent.* 41(2), 106 (2013).
21. H.M. Smith, and A.F. Turner, Vacuum deposited thin films using a ruby laser. *Appl. Opt.* 4(1), 147 (1965).
22. S.N. Ogugua, O.M. Ntwaeaborwa, and H.C. Swart, Latest development on pulsed laser deposited thin films for advanced luminescence applications. *Coatings* 10(11), 1 (2020). https://doi.org/10.3390/coatings10111078.
23. M.A. Fakhri, M.J. AbdulRazzaq, A.A. Alwahib, and W.H. Muttlak, Theoretical study of a pure $LinbO_3$/quartz waveguide coated gold nanorods using supercontinuum laser source. *Opt. Mater.* 109, 110363 (2020).
24. B.P. Swain, and R.O. Dusane, Effect of filament temperature on HWCVD deposited a-SiC: H. *Mater. Lett.* 60(24), 2915 (2006). https://doi.org/10.1016/j.matlet.2005.10.050.
25. Z. Fu, J. Kong, and Q. Qin, Electrochemical and electrochromic properties of niobium oxide thin films fabricated by pulsed laser deposition. *J. Electrochem. Soc.* 146(10), 3914 (1999).
26. R. Ghosh, M.K. Brennaman, T. Uher, M. Ok, E.T. Samulski, L.E. McNeil, T.J. Meyer, and R. Lopez, Nanoforest Nb_2O_5 photoanodes for dye-sensitized solar cells by pulsed laser deposition. *ACS Appl. Mater. Interfaces* 3(10), 3929 (2011).
27. M.A. Fakhri, F.G. Khalid, and E.T. Salim, Influence of annealing temperatures on Nb_2O_5 nanostructures prepared using pulsed laser deposition method. *J. Phys. Conf. Ser.* 1795(1), 12063 (2021).
28. E.T. Salim, S.R. Shafeeq, M.J. AbdulRazzaq, M.A. Fakhri, A.S. Azzahrani, R.K. Ibrahim, and R.A. Ismail, Substrate temperature impact on preparing Nb2O5 Nano-films by IR-Nd: YAG using pulsed laser deposition technique. *J. Opt.* (2023). https://doi.org/10.1007/s12596-023-01545-8.
29. E.T. Salim, S.R. Shafeeq, M.J. AbdulRazzaq, M.A. Fakhri, and S.C.B. Gopinath, Photo-activation of Ag chemicals for enhanced Nb_2O_5 optoelectronic device employing plasmonic effects. *Surf. Interfaces* 36, 102618 (2023). https://doi.org/10.1016/j.surfin.2022.102618.
30. S.R. Shafeeq, E.T. Salim, and M.J. Abdulrazzaq, Q-switched Nd: YAG fundamental and second harmonic wavelengths impact on preparing Nb_2O_5 thin films by a PLD technique: a comparative study. *Int. J. Nanoelectron. Mater.* 16(3), 575 (2023).
31. P. Bibhu, Swain, Influence of process pressure on HW-CVD deposited a-SiC: H films. *Surf. Coat. Technol.* 201(3–4), 1132 (2006). https://doi.org/10.1016/j.surfcoat.2006.01.059.
32. M.A. Fakhri, E.T. Salim, A.W. Abdulwahhab, U. Hashim, M.A. Munshid, and Z.T. Salim, The effect of annealing temperature on optical and photoluminescence properties of $LiNbO_3$. *Surf. Rev. Lett.* 26(10), 1950068 (2019).
33. E.T. Salim, R.A. Ismail, and H.T. Halbos, Growth of Nb_2O_5 film using hydrothermal method: effect of Nb concentration on physical properties. *Mater. Res. Express.* 6(11), 116429 (2019).
34. H. Asady, E.T. Salim, and R.A. Ismail, Some critical issues on the structural properties of Nb_2O_5 nanostructure film deposited by hydrothermal technique. *AIP Conf. Proc.* 2213(1), 20183 (2020).
35. M.A. Fakhri, E.T. Salim, M.H. Wahid, A.W. Abdulwahhab, Z.T. Salim, and U. Hashim, Heat treatment assisted-spin coating for $LiNbO_3$ films preparation: their physical properties. *J. Phys. Chem. Solids* 1(131), 180 (2019).
36. E.T. Salim, M.A. Fakhri, R.A. Ismail, A.W. Abdulwahhab, Z.T. Salim, M.A. Munshid, and U. Hashim, Effect of light induced heat treatment on the structural and morphological properties of Linbo3 thin films. *Super Lattices Microstruct.* 1(128), 67 (2019).
37. M. Abood, E.T. Salim, and J.A. Saimon, Optical investigations of Nb2O5 at different teamperatures for optoelectronic devices. *J. Ovonic Res.* 15(2), 109 (2019).
38. B. Parveen, Z. Khalid, S. Riaz, and S. Naseem, Room-temperature ferromagnetism in Ni-doped TiO_2 diluted magnetic semiconductor thin films. *J. Appl. Res. Technol.* 15(2), 132 (2017).
39. M.A. Fakhri, E.T. Salim, M.H.A. Wahid, A.W. Abdulwahhab, U. Hashim, and Z.T. Salim, Efficiency enhancement of optical strip waveguide by the effect of heat treatment. *Optik* 180, 768 (2019).
40. E.T. Salim, J.A. Saimon, M.K. Abood, and M.A. Fakhri, Electrical conductivity inversion for Nb_2O_5 nanostructure thin films at different temperatures. *Mater. Res. Express* 6(12), 126459 (2019).
41. M.A. Fakhri, M.H. Wahid, B.A. Badr, S.M. Kadhim, E.T. Salim, U. Hashim, and Z.T. Salim, Enhancement of lithium niobate nanophotonic structures via spin-coating technique for optical waveguides application. *Eur. Phys. J. Conf.* 162(7), 01004 (2017).
42. E.T. Salim, M.A. Fakhri, Z. Tareq, and U. Hashim, Electrical and electronic properties of lithium based thin film for photonic application. *AIP Conf. Proc.* 2213(1), 20230 (2020).
43. S.M. Taleb, M.A. Fakhri, and S.A. Adnanm, Optical investigations of nanophotonic $LiNbO_3$ films deposited by pulsed laser deposition method. *Defect Diffus. Forum* 398, 16 (2020).
44. J. Tauc, and A. Menth, States in the gap. *J. Non Cryst. Solids* 8, 569 (1972).
45. E.T. Salim, J.A. Saimon, M.K. Abood, and M.A. Fakhri, Effect of ammonium concentration on structural, optical and morphological

properties of H-Nb_2O_5 thin films—a novel study. *Mater. Res. Express.* 6(4), 046420 (2019).
46. M.K. Abood, M.H. Wahid, E.T. Salim, and J.A. Saimon, Niobium pentoxide thin films employ simple colloidal suspension at low preparation temperature. *Eur. Phys. J. Conf.* 162(12), 01058 (2017). https://doi.org/10.1051/epjconf/201716201058.
47. D. B. Chrisey and G. K. Hubler, "Pulsed laser deposition of thin films," (1994).
48. D.B. Geohegan, *Diagnostic and Characteristics of Pulsed Laser Deposition Laser Plasmas From Pulsed Laser Deposition of thin Films* (New York: Wiley, 1994).
49. S.M. Taleb, M.A. Fakhri, and S.A. Adnan, Physical investigations of nanophotonic $LiNbO_3$ films for photonic applications. *J. Ovonic Res.* 15(4), 261 (2019).
50. A. Miotello, and R. Kelly, Laser-induced phase explosion: new physical problems when a condensed phase approaches the thermodynamic critical temperature. *Appl. Phys. A* 69(1), S67 (1999).
51. B.P. Swain, and R.O. Dusane, Effect of substrate temperature on HWCVD deposited a-SiC: H film. *Mater. Lett.* 61(25), 4731 (2007). https://doi.org/10.1016/j.matlet.2007.03.029.
52. Y. Al-Douri, M.A. Fakhri, N. Badi, and C.H. Voon, Effect of stirring time on the structural parameters of nanophotonic $LiNbO_3$ deposited by spin-coating technique. *Optik* 156, 886 (2018).
53. M.R. Joya, J.J. Barba Ortega, A.M. Raba Paez, J.G. da Silva Filho, and P.D. Cavalcante Freire, Synthesis and characterization of nano-particles of niobium pentoxide with orthorhombic symmetry. *Metals* 7(4), 142 (2017).
54. Z. Guan, Q. Li, H. Zhang, P. Shen, L. Zheng, S. Chu, C. Park, X. Hong, R. Liu, and P. Wang, Pressure induced transformation and subsequent amorphization of monoclinic Nb_2O_5 and its effect on optical properties. *J. Phys. Condens. Matter* 31(10), 105401 (2019).
55. K. Skrodczky, M.M. Antunes, X. Han, S. Santangelo, G. Scholz, A.A. Valente, N. Pinna, and P.A. Russo, Niobium pentoxide nanomaterials with distorted structures as efficient acid catalysts. *Commun. Chem.* 2(1), 1 (2019).
56. N. Sidorov, K. Bormanis, M. Palatnikov, and O. Shcherbina, Determination of niobium-oxygen bond distances and bond orders by Raman spectroscopy. *Solid State Ionics* 45(3–4), 201 (1991).
57. Y. Al-Douri, A. Makram, A. Fakhri, R. Bouhemadou, and M.A. Khenata, Stirrer time effect on optical properties of nanophotonic $LiNbO_3$. *Mater. Chem. Phys.* 203, 243 (2018).
58. M. Palatnikov, O. Shcherbina, N. Sidorov, and K. Bormanis, The structure of niobium and tantalum oxides processed by concentrated light flux. *Ukr. J. Phys. Opt.* 13(4), 207 (2012).
59. X. Wang, Z. Chen, F. Zhang, K. Saito, T. Tanaka, M. Nishio, and Q. Guo, Temperature dependence of Raman scattering in β-(AlGa) 2O3 thin films. *AIP Adv.* 6(1), 15111 (2016).
60. M.A. Fakhri, Y. Al-Douri, and U. Hashim, Fabricated optical strip waveguide of nanophotonics lithium niobate. *IEEE Photonics J.* 8(2), 4500410 (2016).
61. K.S. Khashan, R.A. Ismail, and R.O. Mahdi, Synthesis of SiC nanoparticles by SHG 532 nm Nd: YAG laser ablation of silicon in ethanol. *Appl. Phys. A* 124(6), 443 (2018).
62. M.A. Fakhri, A.W. Abdulwahhab, M.A. Dawood, A.Q. Raheema, N.H. Numan, F.G. Khalid, and E.T. Salim, Optical investigations of nano lithium niobate deposited by spray pyrolysis technique with injection of Li_2CO_3 and Nb_2O_5 as raw materials. *Int. J. Nanoelectron. Mater.* 11, 103 (2018).
63. K. Xu, Silicon electro-optic micro-modulator fabricated in standard CMOS technology as components for all silicon monolithic integrated optoelectronic systems. *J. Micromech. Microeng.* 31(5), 054001 (2021). https://doi.org/10.1088/1361-6439/abf333.
64. R.A. Ismail, K.S. Khashan, and R.O. Mahdi, Characterization of high photosensitivity nanostructured 4H-SiC/p-Si heterostructure prepared by laser ablation of silicon in ethanol. *Mater. Sci. Semicond. Process.* 68, 252 (2017).
65. B. Boruah, R. Gupta, J.M. Modak, and G. Madras, Enhanced photocatalysis and bacterial inhibition in Nb_2O_5 via versatile doping with metals (Sr, Y, Zr, and Ag): a critical assessment. *Nanoscale Adv.* 1(7), 2748 (2019).
66. Y. Wang et al., Strain-induced direct–indirect bandgap transition and phonon modulation in monolayer WS2. *Nano Res.* 8(8), 2562 (2015).
67. R.A. Ismail, A.M. Al-Samarai, and A.M. Muhammed, High-performance nanostructured p-Cu2S/n-Si photodetector prepared by chemical bath deposition technique. *J. Mater. Sci. Mater. Electron.* 30(12), 11807 (2019).
68. P.R. Willmott, and J.R. Huber, Pulsed laser vaporization and deposition. *Rev. Mod. Phys.* 72(1), 315 (2000).
69. S.A. Abid, A.A. Taha, R.A. Ismail et al., Antibacterial and cytotoxic activities of cerium oxide nanoparticles prepared by laser ablation in liquid. *Environ. Sci. Pollut. Res.* 27, 30479 (2020). https://doi.org/10.1007/s11356-020-09332-9.
70. M.K. Abood, E.T. Salim, and J.A. Saimon, Impact of substrate type on the microstructure of H-Nb_2O_5 thin film at room temperature. *Int. J. Nanoelectron. Mater.* 11, 55 (2018).
71. R.A. Ismail, Fabrication and characterization of photodetector based on porous silicon. *E-J. Surf. Sci. Nanotechnol.* 20(8), 388 (2010).